AIAA JOURNAL
Vol. 40, No. 11, November 2002

Numerical Investigations on Dynamics and Heat Transfer in a Turbulent Underexpanded Jet

Yann Bartosiewicz,* Yves Mercadier,† and Pierre Proulx‡
Université de Sherbrooke, Sherbrooke, Québec J1K2R1, Canada

A fully elliptic Navier–Stokes equation solver in conjunction with a Reynolds stress model is validated for mildly and strongly underexpanded jets. For mildly underexpanded jets, good agreement has been found compared to available measurements for the shock reflections. The model even demonstrated some improvements over a three-dimensional modified k–ϵ model for turbulent predictions, which confirms the inadequacy of isotropic eddy-viscosity-based models to represent properly the turbulence in those flows. For the strongly underexpanded case, the predicted Mach disk location and size are found to be in excellent agreement compared to available measurements. In addition, the predicted flow structure beyond the disk agrees with experimental observations. An attempt is also made to explain the strong coupling between some dynamic features and heat transfer aspects. The sonic line location is revealed to be an important parameter in understanding the global dynamics/heat transfer coupling. In addition, it is demonstrated that a fraction of heat dissipation may be given back to the flow and boost its temperature, which may be useful for spraying applications.

Nomenclature

a	=	sound speed, m/s
C_p	=	specific heat, J/K · kg
D	=	nozzle exit diameter or jet diameter, m
dq	=	heat quantity, J/m^3
E	=	total energy, J/kg
$I_{\%}$	=	turbulent intensity
k	=	turbulent kinetic energy, m^2/s^2
M	=	Mach number
P	=	static pressure, Pa
R	=	nozzle exit radius or jet radius, m
r	=	gas constant, J/K · kg
T	=	static temperature, K
T_t	=	jet total temperature, K
U	=	mean velocity, m/s
u	=	axial velocity, m/s
u'	=	fluctuating axial velocity, m/s
v	=	radial velocity, m/s
v'	=	fluctuating radial velocity m/s
X	=	axial position, m
Y	=	radial position, m
α	=	thermal conductivity, W/m · K
δ_{ij}	=	Kronecker symbol
ϵ	=	turbulent dissipation rate, m^2/s^3
μ	=	molecular viscosity, kg/m · s
μ_{eff}	=	effective viscosity, kg/m · s
μ_t	=	turbulent viscosity, kg/m · s
ρ	=	mass density, kg/m^3

Subscripts

a	=	ambient or coflow
e	=	nozzle exit
s	=	along the sonic line

Received 8 June 2001; accepted for publication 15 April 2002.

*Ph.D. Student, Engineering Faculty, Department of Mechanical Engineering.
†Professor, Engineering Faculty, Department of Mechanical Engineering.
‡Professor, Engineering Faculty, Department of Chemical Engineering.

I. Introduction

UNDEREXPANDED, axisymmetric freejets are simple flows involving some complex phenomena such as turbulent mixing, compressibility effects, and heat transfer coupling. Therefore, knowledge of the dynamic and energetic features of underexpanded jets is very useful in many engineering tools. The ability to predict the detailed structure of such flows has a wide range of practical applications such as the design of rocket exhausts,[1] fuel injectors,[2] and vehicle maneuvering thrusters, and the consequences and risk assessment[3,4] of leaks of high-pressure gases or shock noise features.[5] Of particular interest in the present work is the use of such prediction methods to jets employed for plasma spraying applications.[6] Knowledge of the dynamic and energetic structures existing in this flow type is potentially useful for the plasma jets created by dc plasma torch[7] and may also be useful for the optimization of particles injection or the position of the spray receiving substrate. Depending on the pressure ratio P_e/P_a, the jet may present different topologies and structures, and it may be called either mildly underexpanded or strongly underexpanded.

Many studies have been carried out on this subject since the 1980s. Most of the previous studies[3,4,8–10] were devoted to turbulence and physical model validation, and they were only focused on the shock's location/amplitude and their size being relatively simple to measure directly. Consequently, other features or potential applications of these underexpanded jets were often neglected. However, some studies examined new features such as shock reflection hysteresis[11] or shock noise.[5] For the turbulence modeling, most rely on various two-point closure models such as k–ϵ or $k-\omega$ with an aditional compressibility correction[3–5,8,10] or a multiscale effect.[9] Nevertheless, those models are still limited for axisymmetric flows,[12,13] and they are not suited for the entire jet flow computation. They rely on the Boussinesq hypothesis, which supposes that turbulent kinetic energy is equally distributed to all fluctuating velocity components. However, it is known that the axial turbulence intensity is larger than the others. Even with a compressibility correction, the k–ϵ model is too dissipative and provides too smoothed shocks and a slight phase error in their location[3,10] without making some ajustments or empirical calibrations.[3] However, with a three-dimensional computation, it seems that these errors are smoothed away and the compressibility corrected k–ϵ model, with its standard constants, provides reasonably good results in the near-field region (up to $X/R \sim 40$) for the location of the shock cells[8] for both types of underexepanded jets: This effort, however, leads to substantial increases in memory and CPU time requirements. In addition, even if the k–ϵ model is able to give acceptable results for the mean flowfield, it has been proven that it provides some inconsistencies or nonphysical results for turbulence

predictions.[14,15] For numerical models, although some authors use Euler equations[16,17] and/or parabolized models,[8–10] the elliptic version of the full Naviers–Stokes equations seems better suited for general application to a wide range of jets (sonic release).[3,4,18] In addition, finite volume discretization, upwind schemes,[8] time-marching techniques,[3,4,8] and grid adaptation[8,17] all contribute to capture shocks accurately and to reduce the numerical diffusion.

A major failure of most previous numerical as well as experimental studies is the lack of any detailed knowledge about heat transfer phenomena and their coupling with the dynamic characteristics of these kinds of flows. Only Dash et al.[10] reported a faster mixing observed for a hot jet in comparison to a cold one, but no detailed study was conducted on heat transfer aspects and the parameters that drive them.

The current study is a primary work to understand the strong coupling between the compressibility, turbulence, and heat transfer in underexpanded air jets. Knowledge of dynamic and energetic features of underexpanded simple gas jets is necessary to afford more complex gas mixtures. The objective of this work is to set up a robust model for the simulation of underexpanded turbulent plasma jets where the gas may be considered as a mixture of electrons, ions, and atoms and where measurements become more difficult. First, code validation for both mildly and strongly underexpanded jets is explored. For both cases, the numerical predictions are compared to available experimental data, or other numerical and theoretical studies. Then, because no extensive study of heat transfer has been completely achieved in the past studies, the focus is turned to that aspect. The influence of the jet temperature on the turbulent dynamics is investigated. Finally, a heat transfer feature and its coupling with the dynamic characteristics of these jets is studied.

II. General Description of an Underexpanded Jet

The flow pattern of a jet issuing from a convergent nozzle depends primarily on the pressure ratio at the nozzle exit. Basically, three types of flows are possible, depending on this ratio. If the pressure ratio is exactly one ($P_e/P_a = 1$), the jet is fully expanded and no shock occurs. If the pressure ratio is in the range P_e/P_a from 1.1 to 2.1, the jet is said to be mildly underexpanded (Fig. 1a). This pressure difference is resolved locally across an expansion wave network from the nozzle edge and compression waves that involve oblique shocks. The expansion waves are reflected as compression waves from the constant pressure free boundary, giving rise to a multicell barrel-shaped structure. For a high enough pressure ratio, these compression waves coalesce to form an axisymmetric curved shock, which propagates across the centerline (Fig. 1a). Many experimental[5] or numerical[3,4,8] studies have been carried out on such flows, and they were generally focused on the mean flow dynamics and the ability to predict shock waves spacing and decay.

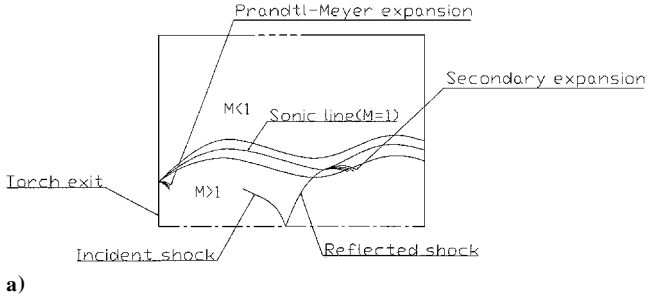

a)

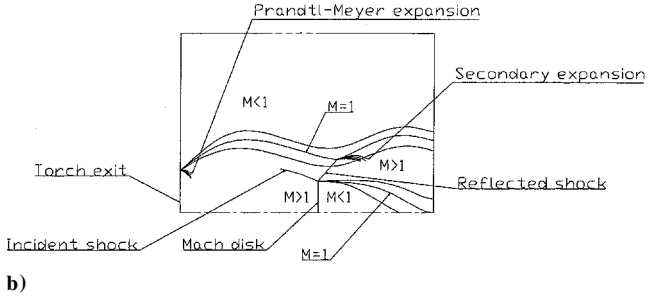

b)

Fig. 1 Underexpanded jet configurations: a) mildly and b) strongly.

For higher pressure ratios, the distance separating the incident and the reflected shocks decreases so much that a normal shock is formed around the centerline and is called a Mach disk. Figure 1b shows this flow configuration. Downstream of the Mach disk, the flow becomes subsonic and is bounded by a slip stream emanating from the triple point and may or may not become supersonic again depending on the pressure ratio. For these jets, many experimental[19] as well as theoretical[20–22] (characteristic method) or numerical[8,17] investigations have been conducted. Most of them[8,17] dealt with the Mach disk location and size. [An experimental investigation was also carried out by C. Peters, Arnold Engineering Development Center, Arnold Air Force Base, Tennesee, in 1973 (private communication).]

The supersonic/subsonic region is delimited by the sonic line ($M = 1$ in Figs. 1a and 1b). This constant pressure free boundary represents shock wave terminations.[5,21] In the near-field region, its location increases because the jet tends to accelerate due to its underexpanded nature; the sonic condition is then closer to the coflow (here a subsonic coflow) than the jet. However, as the jet decelerates downstream because of viscous mixing, there exists a point where the jet becomes closer to the sonic condition than the outer flow does. The sonic line location starts to decrease and reaches the axis, where the jet becomes exactly sonic. Moreover, as this line is the termination point of shock reflection, it is responsible for the shock cell spacing.[5]

III. Mathematical Models

Governing Equations

The flow from a circular nozzle is governed by the steady-state, axisymmetric form of the fluid flow conservation equations. For brevity, these equations will be expressed in Cartesian tensor form. For variable density flows, the Favre averaged Navier–Stokes equations are more suitable and can be written for the mass, momentum, and energy conservation.

Continuity:

$$\frac{\partial \rho}{\partial t} + \frac{\partial}{\partial x_i}(\rho u_i) = 0 \tag{1}$$

Momentum:

$$\rho \frac{\mathrm{D}u_i}{\mathrm{D}t} = -\frac{\partial P}{\partial x_i} + \frac{\partial}{\partial x_j}\left[\mu_{\text{eff}}\left(\frac{\partial u_i}{\partial x_j} + \frac{\partial u_j}{\partial x_i} - \frac{2}{3}\delta_{ij}\frac{\partial u_k}{\partial x_k}\right)\right] + \frac{\partial}{\partial x_j}(-\rho\overline{u_i' u_j'}) \tag{2}$$

with the velocity representing the mass-averaged values.

The turbulent heat transport is modeled using the Reynolds analogy to turbulent momentum transfer. The modeled energy equation is, thus,

$$\frac{\partial}{\partial t}(\rho E) + \frac{\partial}{\partial x_i}[u_i(\rho E + P)] = \frac{\partial}{\partial x_i}\left[\left(\alpha + \frac{C_p \mu_t}{P_{rt}}\right)\frac{\partial T}{\partial x_i} + u_j(\tau_{ij})_{\text{eff}}\right] \tag{3}$$

where E and T are the mass-averaged values and (τ_{ij}) is the stress tensor, defined as

$$(\tau_{ij}) = \mu_{\text{eff}}\left(\frac{\partial u_j}{\partial x_i} + \frac{\partial u_i}{\partial x_j}\right) - \frac{2}{3}\mu_{\text{eff}}\frac{\partial u_i}{\partial x_i}\delta_{ij} \tag{4}$$

The term τ_{ij} is the viscous heating due to the dissipation. The default value of the turbulent Prandtl number P_{rt} is set to 0.85. The turbulent viscosity μ_t is computed similarly to the k–ϵ model ($C_\mu = 0.09$):

$$\mu_t = \rho C_\mu (k^2/\epsilon) \tag{5}$$

The equation of state for perfect gases is added to close the system:

$$P/\rho = rT \tag{6}$$

The temperature dependence of the transport and thermodynamic properties has been taken into account because shocks may involve large temperature gradients. All of the properties, C_p, μ, and k, are evaluated by means of a sixth-order polynomial curve fitting[23] from the tables of air properties.[24] These laws are accurate to within approximately $\pm 2\%$ of the value listed in the tables for a temperature range between 100 and 2500 K.

Turbulence Modeling

In a recent paper,[25] several second-moment-order closure models have been compared with the Reynolds stress model (RSM), especially for the mildly underexpanded jet. All of the tests were performed with the published constants. The RSM has been found to do the best overall job, even though some further tests were needed for the strongly underexpanded case. This is a more elaborate turbulence model in so far as an isotropic eddy viscosity (Boussinesq hypothesis) is no longer assumed. Nevertheless, its cost in computation time may be more important than simpler models because it adds four additionnal equations in two dimensions, but this drawback is overcome by a good k–ϵ initilization. The RSM used in the present work may be expressed in a simple form as

$$\frac{\partial}{\partial t}(\rho\overline{u_i'u_j'}) + \frac{\partial}{\partial x_k}(u_k\rho\overline{u_i'u_j'}) = D_{ij}^T + D_{ij}^L + P_{ij} + \phi_{ij} + \epsilon_{ij} \quad (7)$$

where D_{ij}^T, D_{ij}^L, P_{ij}, ϕ_{ij}, and ϵ_{ij} are the turbulent diffusion, the molecular diffusion, the stress production, the pressure strain, and the dissipation. Of the various terms in these exact equations, D_{ij}^L and P_{ij} do not require any modeling. They can be written as

$$D_{ij}^L = \frac{\partial}{\partial x_k}\left[\mu\frac{\partial}{\partial x_k}(\overline{u_iu_j})\right] \quad (8)$$

$$P_{ij} = -\rho\left(\overline{u_iu_k}\frac{\partial u_j}{\partial x_k} + \overline{u_ju_k}\frac{\partial u_i}{\partial x_k}\right) \quad (9)$$

Unfortunately, several terms in the exact equations are unknown, and modeling assumptions are required to close the system. These terms are D_{ij}^T, ϕ_{ij}, and ϵ_{ij}, and they are written in the exact equations as

$$D_{ij}^T = -\frac{\partial}{\partial x_k}[\rho\overline{u_iu_ju_k} + \overline{P(\delta_{kj}u_i + \delta_{ik}u_j)}] \quad (10)$$

$$\phi_{ij} = \overline{P\left(\frac{\partial u_i}{\partial x_j} + \frac{\partial u_j}{\partial x_i}\right)} \quad (11)$$

$$\epsilon_{ij} = -2\mu\overline{\frac{\partial u_i}{\partial x_k}\frac{\partial u_j}{\partial x_k}} \quad (12)$$

The complete modeling details of the term D_{ij}^T and ϕ_{ij} may be found in Refs. 26 and 27. The dissipation rate ϵ_{ij} is computed by a transport equation identical to that used in a k–ϵ model. Moreover, a dilatation–dissipation term is added to the ϵ expression, according to Sarkar and Balakrishnan[28] and Sarkar et al.[29] proposals, to take into account the reduced spreading rate observed in compressible mixing layers[30]:

$$\epsilon_{ij} = \tfrac{2}{3}\delta_{ij}(\rho\epsilon + Y_M) \quad (13)$$

where $Y_M = 2\rho\epsilon M_t^2$. The turbulent Mach number M_t is defined as $M_t = \sqrt{(k/a^2)}$. The turbulent kinetic energy is obtained by taking the trace of the Reynolds stress tensor $k = \frac{1}{2}\overline{u_i'u_i'}$. For the Reynolds stress boundary conditions, it is difficult to set directly the stresses at a flow inlet. An alternate method is to make the assumption of turbulence isotropy and, thus, compute the stresses from the turbulent kinetic energy:

$$\overline{u_i'^2} = \tfrac{2}{3}k \quad (14)$$

$$\overline{u_i'u_j'} = 0 \quad (15)$$

The boundary values of k and ϵ, thus, may be obtained from the turbulence intensity and turbulent viscosity ratio. For instance, a tubulence intensity of 5% and a turbulent viscosity ratio of about 2 are typical of a fully developed turbulence in a pipe.

Computational Procedure

Integration of the conservation equations (continuity, momentum, and energy) was performed using a second-order finite volume scheme. Consequently, the equations are discretized following a conservative finite volume technique, with values of the dependent variables stored at the cell centers of the computational mesh. Diffusion and source terms are computed using a second-order central difference. The inviscid fluxes are derived using a second-order flux difference splitting.[31] The latter technique is derived from conventional Roe's flux splitting,[32] where the system was a time derivative preconditioned to rescale its eigenvalues to overcome the numerical stiffness encountered at low Mach numbers. The inviscid terms in the Roe scheme are cast in the form of an approximate Riemann problem. The interface flux is determined by separate terms, which depend on the quantities on the upstream and downstream sides of the face. The current form of the inviscid fluxes at each interface can be viewed as a second-order central difference plus an added matrix dissipation. This latter term allows an upwinding required for stability, and the information passed through the face contains the flow characteristics. The detailed procedure of the flux splitting may be found in Refs. 31 and 32.

Other scalar equations, such as turbulence, are discretized by the same technique (second-order central difference for the diffusion terms and second-order upwind scheme for the advection term), but solved separately, whereas the governing equations are solved with a couple approach. The linearized implicit scheme is then obtained, using an Euler implicit discretization in time, in conjunction with a Newton-type linearization of the fluxes.[33] The resulting block system is solved using a point Gauss–Seidel scheme. The desired steady state is obtained using a time-marching approach, where the time step is set up by a Courant–Friedrichs–Lewy (CFL) number.

Numerical Accuracy

The criterion for assessing convergence was based on the root mean square of the density residues expressed by

$$R(\rho) = \sqrt{\sum_{i=1}^{N}\left(\frac{\partial\rho}{\partial t}\right)_i^2} \leq 1 \times 10^{-8} \quad (16)$$

where N is the number of grid points. At convergence, the mass imbalance applied to the whole domain is

$$\left|\frac{\sum \dot{m}_{\text{in}} - \sum \dot{m}_{\text{out}}}{\sum \dot{m}_{\text{in}}}\right| \leq 1 \times 10^{-5} \quad (17)$$

In the same way, the total energy imbalance is checked and is about 1×10^{-4}.

During the first iterations, the CFL number is set to 0.5 because changes in the solution are highly nonlinear, and it is progressively increased as the solution progresses. Its maximum may be larger than 1 (with 4 the maximum value reached) due to the linear stability theory for implicit schemes.

In this work, a triangular mesh is used in conjunction with an adaptative procedure following the Mach number and density gradients.[34] This method is unavoidable because the shock reflection location may vary widely with the operating conditions. Nevertheless, a grid-convergence study has been made to check the axial and radial accuracy of the final mesh. The final grid has shown less than 5% of difference with the previous adaptation step for axial and radial Mach profiles (not shown). Once adapted, the computational domain (Fig. 2) has about 30,000 cells.

IV. Computational Domain and Boundary Conditions

Figure 2a shows the general dc plasma spraying system, the particular interest of the present work. The plasma is formed between

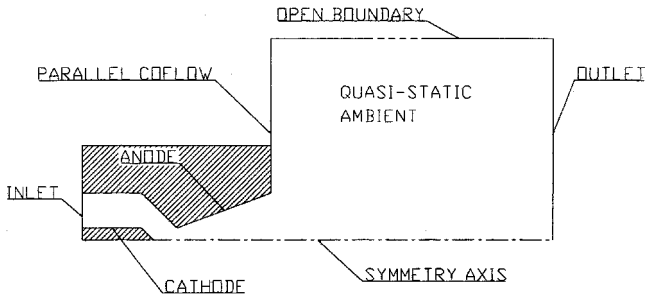

a)

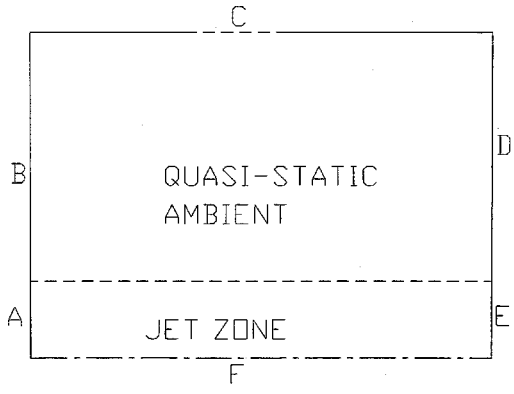

b)

Fig. 2 Computational domain and boundary conditions.

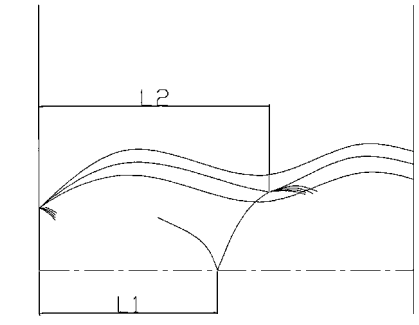

a)

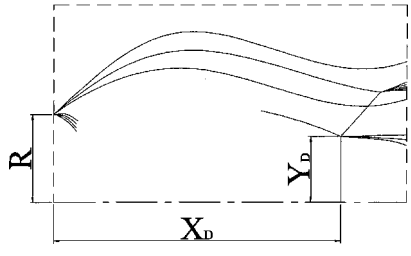

b)

Fig. 3 Shock reflection lengths.

the anode and cathode and then acelerated through a convergent–divergent nozzle. The supersonic jet may be used, for instance, to spray some specific particles to coat a surface. Nevertheless, in the present study, the plasma generation device will not be modeled because the complex coupling between dynamics and heat transfer occurring in simpler gas flows must first be understood. The computational domain is an axisymmetric rectangle (Fig. 2b). The initial jet radius is equal to that of the exit nozzle (1 cm). The outer boundary is located 7 radii from the jet lipline in the transverse direction and 40 radii in the streamwise direction and will be extended to 80 radii for the heat transfer study. In Fig. 2, condition A is the nozzle exit: At this inlet boundary, all of the flow properties are imposed because the incoming flow is supersonic. Boundary conditions B and C denote a parallel coflow, which may be subsonic or supersonic. At

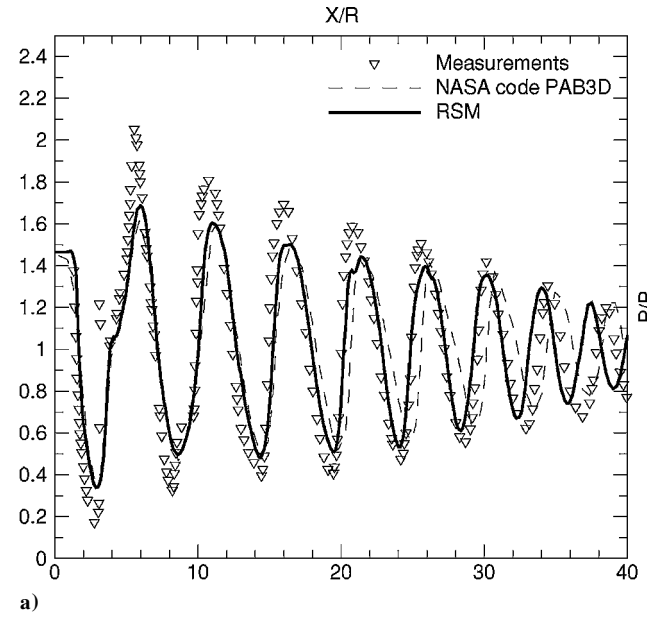

a)

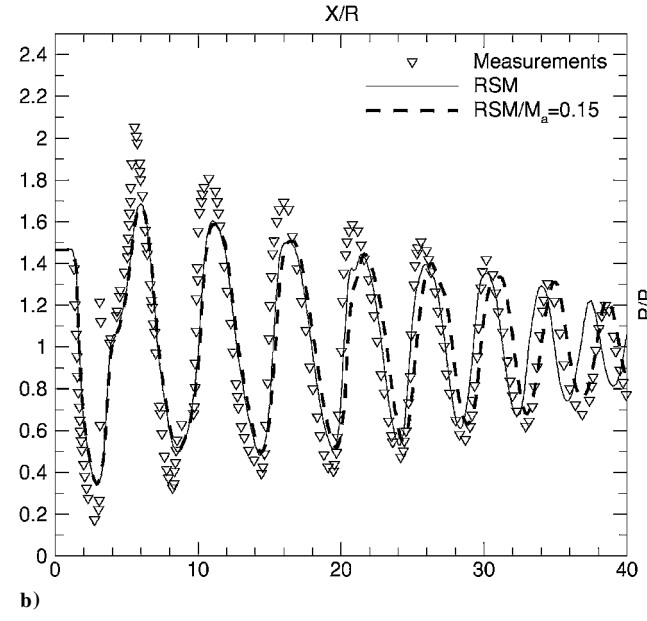

b)

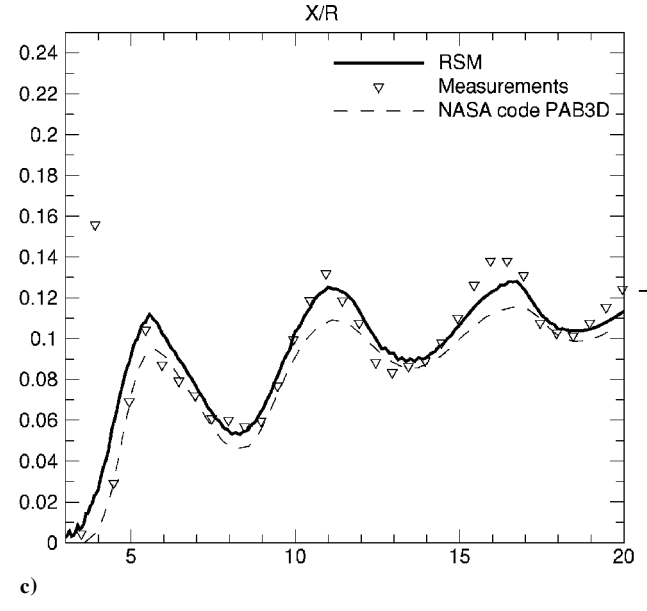

c)

Fig. 4 Axial pressure and axial turbulent intensity.

F, a symmetry condition is applied with $\boldsymbol{n} \cdot \boldsymbol{v} = 0$. Conditions D and E are outlet conditions, which depend on the flow characteristics. If the flow is subsonic, ambient pressure with $P_a = 1$ atm is imposed, but if the flow is supersonic, all of the properties will be extrapolated from the interior of the domain. At the inlets, there is a turbulent intensity of 5%, and a turbulent viscosity ratio is set equal to 2. In this work, the jet static temperature, the pressure ratio, and the coflow Mach number can be ajusted, whereas the ambient pressure is kept to a constant value of 1 atm.

For a good initialized solution, the flow is computed in a first step by a standard k–ϵ model, and the obtained solution is then used for the initialization with the RSM. This method leads to a reduction of the overall computation time.

V. Validation of the Numerical Model

Mildly Underexpanded Jets

For the validation work, only isothermal jets have been simulated to be compared to the available experimental data. In this way, the static temperature of the jet at the nozzle outlet section will be considered the same as the ambient temperature and will be taken to be 300 K: $T_e = T_a = 300$ K. The minimum coflow Mach number is set to 0.001 to ensure numerical stability and may be adjusted if needed.

In this section, a Mach 2 ($M_e = 2$) jet has been simulated for two different pressure ratios. For the first one, P_e/P_a is set to 1.3, and the numerical predictions of the shock's reflection lengths (Fig. 3a) are compared to the measurements of Love et al.[35] For the first reflection, the numerical predictions give $L1/R = 2.75$ vs the measurement $L1/R = 3$, whereas for the second reflection, the present code predicts $L2/R = 5.5$ vs the experimental data $L2/R = 5.2$. Because the maximum error is about 8.3%, it shows that the initial expansion and the sonic line position are properly represented.

For the second jet, the pressure ratio is $P_e/P_a = 1.47$ and matches with that of the experimental work of Dash et al.[5] The results are also compared with those of Pao and Abdol-Hamid[8] obtained with a three-dimensional modified k–ϵ NASA code (PAB3D). Figure 4 shows the predictions for the centerline static pressure (Figs. 4a and 4b) and the longitudinal tubulence intensity (Fig. 4c). From Figs. 4a and 4b, it appears that the first peak is underpredicted by about 15% for the both models, but the difference decreases downstream because the jet no longer experiences the initial conditions. This might be solved if an inviscid model were used in this region.[10] However the RSM seems to give as good or even better results as the three-dimensional modified k–ϵ model up to the location $X/R = 35$ and with a lower CPU time and memory requirement than a three-dimensional simulation. For the last shock cell, a slight phase error is observed, which may be attributed to the proximity of the outlet condition. Dash et al.[5] reported this observation in their code and attributed it to a velocity entrainment-inducedeffect.

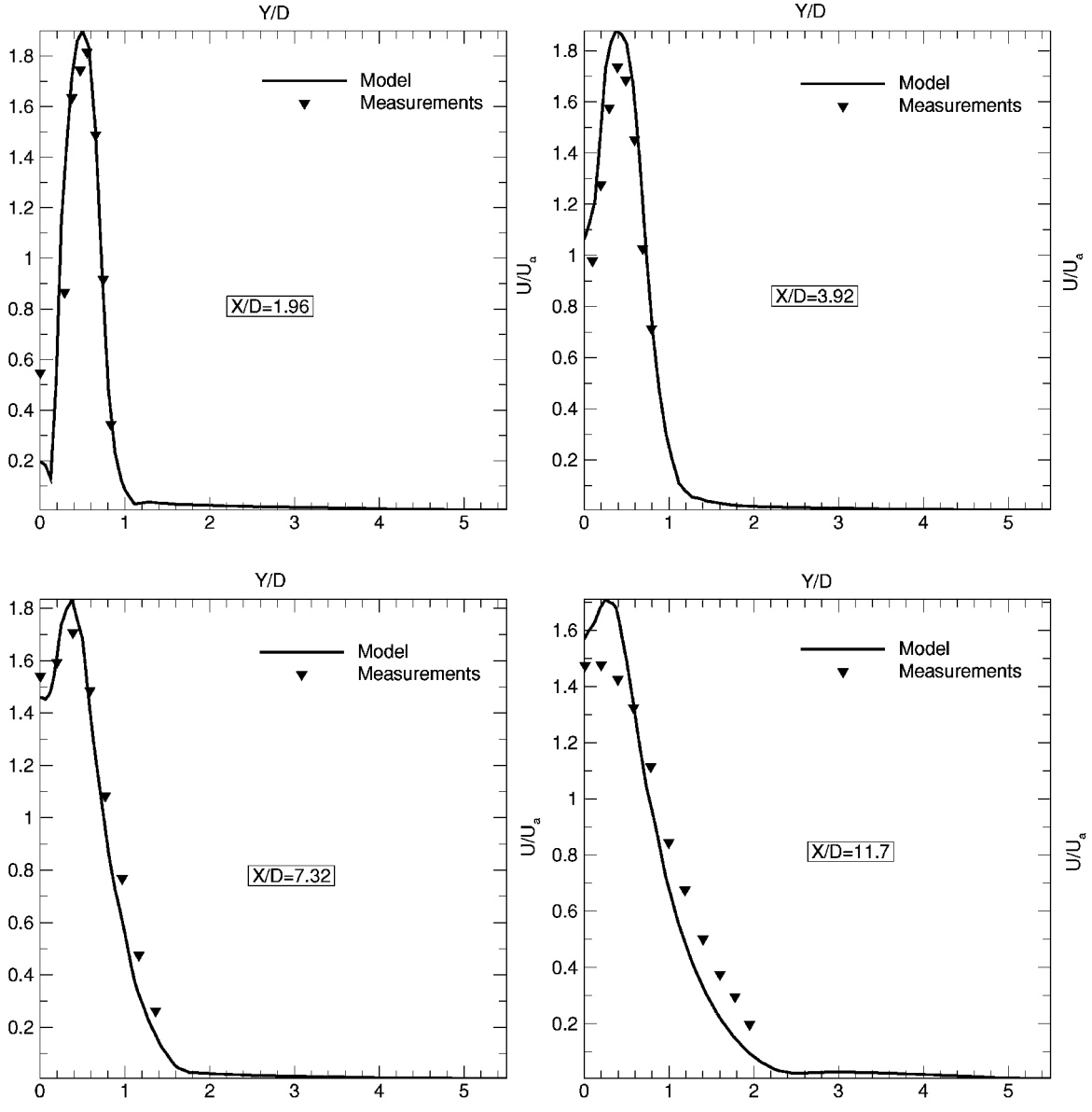

Fig. 5 Mean streamwise velocity profiles at different axial stations.

Table 1 Mach disk location and size

	Case 1[17,36]		Case 2[20,36a]		Case 3[20,36a]		Case 4[4,19,36]	
Method	X_d/R	Y_d/R	X_d/R	Y_d/R	X_d/R	Y_d/R	X_d/R	Y_d/R
Numerical	4.62	1.1	——	——	——	——	3.36	0.62
Theoritical	——	——	9.88	1.27	13.06	2.22	——	——
Empiric formula	4.7	——	12.67	——	17.3	——	3.5	——
Measurements	——	——	9.92	——	13.16	——	3.16	0.59
RSM	4.8	1.05	10.2	1.25	13.3	2.11	3.33	0.6

[a]Private communication, C. Peters.

Figure 4b shows the influence of the coflow Mach number, which has been set to 0.15. As already observed by Dash et al.,[5] the near-field region is not influenced by the coflow properties, unlike the region $X/R > 35$, where the shock spacing and strength is changed. They also argued that a flight Mach number may solve the problem of the velocity entrainment-induced effect and an $M_a = 0.15$ may be representative for these conditions.[5]

Figure 4c demonstrates that the RSM predicts the axial turbulence intensity $I_{\%} = \sqrt{(u'^2/U_e)}$ along the jet lipline ($Y = R$) better than the k–ϵ model. The maximum error compared to the experimental data is about 7%. This is mainly attributed to k–ϵ models that assume an equally fluctuating velocity distribution and then an isotrope turbulence intensity. Therefore, a directional turbulence intensity should be computed empirically[5] from $k = (u'^2 + v'^2 + w'^2)/2$ with these two-point closure models.

Strongly Underexpanded Jets

For these jets, many experimental[19] as well as theoretical[20–22] (characteristic method) or numerical[8,17] investigations have been conducted. Most of them dealt with the Mach disk location and size (Fig. 3b)[8,17] (also private communication, C. Peters). Four tests have been carried out to validate the model against measurements, theoretical studies, and other numerical results. The Mach numbers for the different cases have been set to 1.01, 2.44, 2.44, and 1, while the matching pressure ratios were 6.69, 5.75, 10.7, and 3.57, respectively. For those tests, just a stabilizing flight Mach number $M_a = 0.001$ has been applied.

The results for the Mach disk location and size (Fig. 3b) are presented in Table 1. The maximum error compared to measurements for the Mach disk location is about 4.4%, and the agreement for the disk size is even better. Table 1 also shows that the empirical formula proposed by Ashkenas and Sherman[36] for the Mach disk location does not give accurate results for relatively high Mach number. Figure 5 shows the comparison between experimental data[19] and the present model, for the flowfield beyond the Mach disk with operating conditions matching with the case 4. The radial profiles of the mean streamwise velocity are compared at different axial stations after the Mach disk (Fig. 5). For the first three stations, the agreement is reasonably good except near the axis, where it is difficult to measure. At $X/D = 1.96$ and $X/D = 3.92$, it is shown that the jet is subsonic and sonic close to the axis region. These predictions illustrate the presence of a subsonic zone behind the disk and the occurrence of a second Mach disk between these two stations, which has been verified experimentally.[19] For the last station, a significant difference is observed between the measured and computed values. Nevertheless, Donaldson and Snedeker[19] stated that their measurements were subjected to the influence of a flapping instability, making the jet oscillate about its mean position and tending to flatten the profiles.

VI. Heat Transfer and Dynamics Coupling

Influence of Jet Temperature on Dynamics

The exit temperature of the jet is changed while the ambient temperature is kept constant, and the goal of this study is to reveal the effects of this change on the turbulent dynamics. However, our primary interest is for hot jets to form the basis of work on more complex, but qualitatively the same,[6] higher temperature flows, such as plasmas. Actually, the jet temperature is progressively increased by boosting the inlet total temperature yet retaining the same Mach

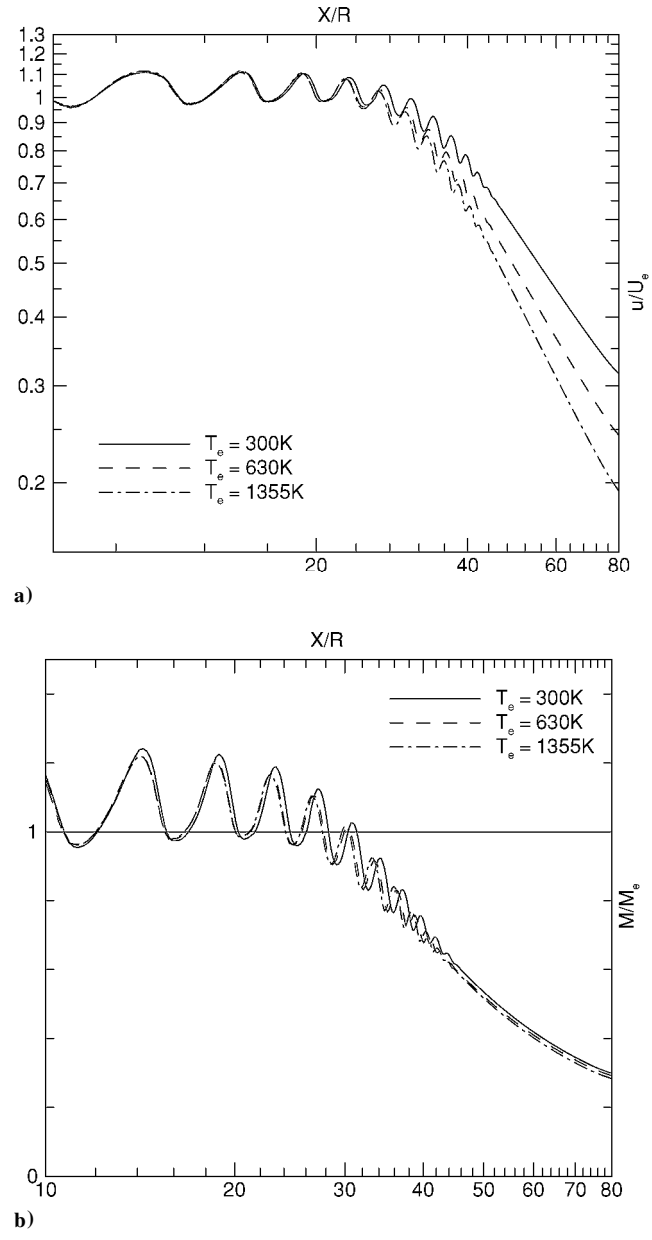

Fig. 6 Nondimensionnal centerline velocity and Mach number.

number. The trial cases were an $M_e = 2$ jet with a pressure ratio $P_e/P_a = 1.3$ and an $M_a = 0.15$ flight Mach number. Three exit temperatures have been tested, 300, 630, and 1355 K, while the coflow temperature is maintained at 300 K. The 300-K jet exhausting into the 300-K ambient will be henceforth described as the isothermal case.

For this test, the dynamics of the shocks reflection has been previously checked. Figure 6 shows the centerline axial velocity and the Mach number. It appears that the initial mixing ends around $X/R = 35$ (Figs. 6 and 7a) for the isothermal case, which agrees well with predictions or experimental observations.[5] In addition, for hot jets, it is shown that the mixing is significantly faster than that in the isothermal case (Fig. 6a). In this case, the initial mixing is up to about $X/R = 30$, and the transition is also faster. That is confirmed by the turbulence level, which is higher for the hot jets in the transition zone at the end of the initial mixing (Fig. 7a). Moreover, it is clear that this transition begins near $X/R \sim 20$ (Fig. 7a). It is also shown that, after this first mixing zone, turbulent kinetic energies are inversely ranked following the jet exit temperature: Indeed, the fluctuating velocity is higher for the isothermal case unlike in the transition zone (Fig. 7a). However, the local turbulence intensity, defined as $\sqrt{(\overline{u'u'} + \overline{v'v'} + \overline{u'v'})}/U$, is still higher for the hot jets. Note that the changes in the dynamics are more important between

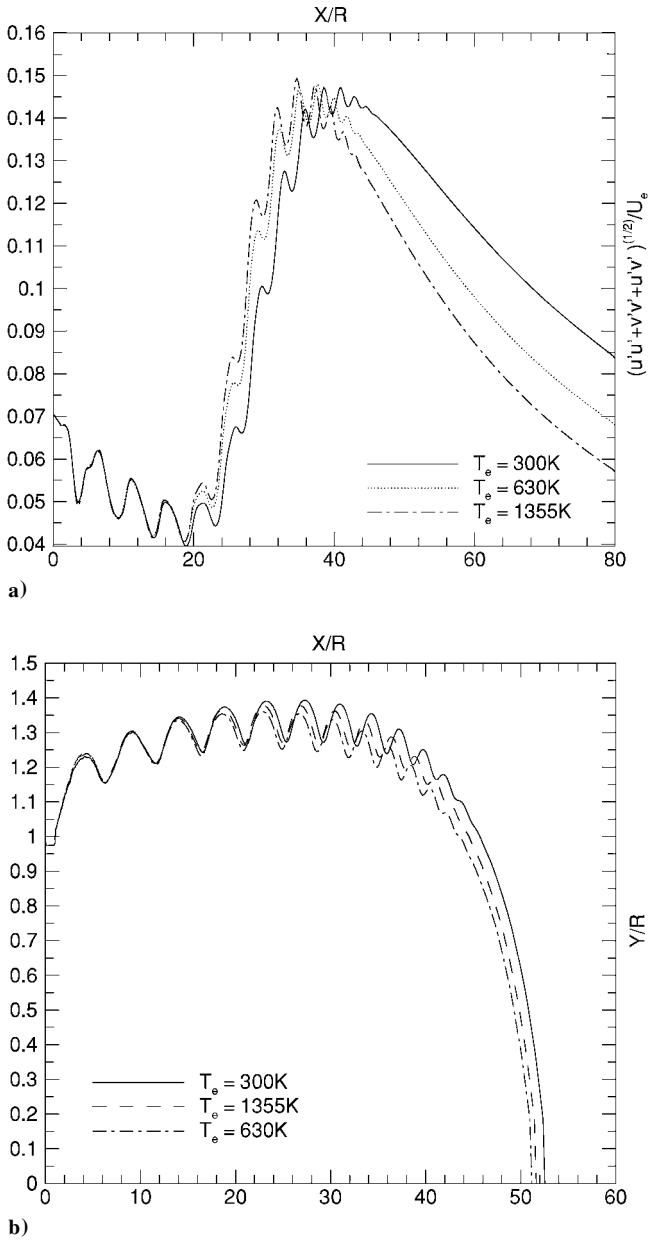

Fig. 7 Evolution of the local Reynolds stresses; sonic line location.

a 300-K jet and a 630-K jet than between the 630-K and the 1355-K jet; this effect is attributed to the changes in the properties of air in this temperature range.

Figure 7b shows the effect of the jet temperature on the sonic line position, which will be revealed as a determining parameter for the dynamics and heat transfer coupling in those flows. The location of this line depends primarily on the difference between $\Delta M_a = M_s - M_a$ and $\Delta M_j = M_j - M_s$, where $M_s = 1$ is the Mach number along the sonic line. In the near-field region, $\Delta M_a > \Delta M_j$, and the sonic line location tends to increase (Fig. 7b) because the sonic condition is closer to the coflow than the jet. Nevertheless, during the transition of the initial mixing, the centerline Mach number decreases, and the condition $\Delta M_a < \Delta M_j$ occurs at approximatively $X/R \sim 32$. From this point, the sonic line location decreases slightly and falls drastically to the axis position (Fig. 7b) from the end of the initial mixing zone (from $X/R \sim 40$ for the isothermal case). At $X/R \sim 52$, the sonic condition reaches the axis (Fig. 7b), and the jet becomes subsonic downstream of this point. In addition, it is shown that, for the hot jets, the sonic line is located below its position for the isothermal case, and a slight dephasing is emphasized from the transition point $X/R \sim 20$ and appears on the centerline Mach number (Fig. 7b).

Heat Transfer Aspects

Figure 8a presents the centerline temperature for the three earlier given jet exit temperatures. It appears that, for the isothermal case, the temperature starts to increase from $X/R \sim 23$ and reaches a value of 348 K at $X/R \sim 52$, which is higher than the exit jet or coflow temperature and even higher than the compression temperature just behind any shock cells. After this maximum value, the temperature decreases to the ambient conditions farther downstream. This feature does not take place for the hotter jets (Fig. 8a), where the temperature decreases normally with the turbulent mixing to reach the ambient value. It is also shown that this phenomenon is related to the sonic line temperature (Fig. 8a). The temperature along this line is a representative value of that in the jet/coflow mixing layer. In this region, the flow reaches a momentum and a thermal equilibrium between the inner jet and the outer coflow. From a thermal point of view, thermal equilibrium is reached between the two flow initial temperatures and the heat generation coming from the kinetic energy, which is transformed into thermal energy through the viscous dissipation. Because the temperature of hot jets is much higher than that of the ambient, the resulting temperature in the mixing layer or along the sonic line is lower than the jet temperature, unlike what happens in the isothermal case. In addition, the sonic line cuts the mixing layer into a subsonic and a supersonic part. Because the

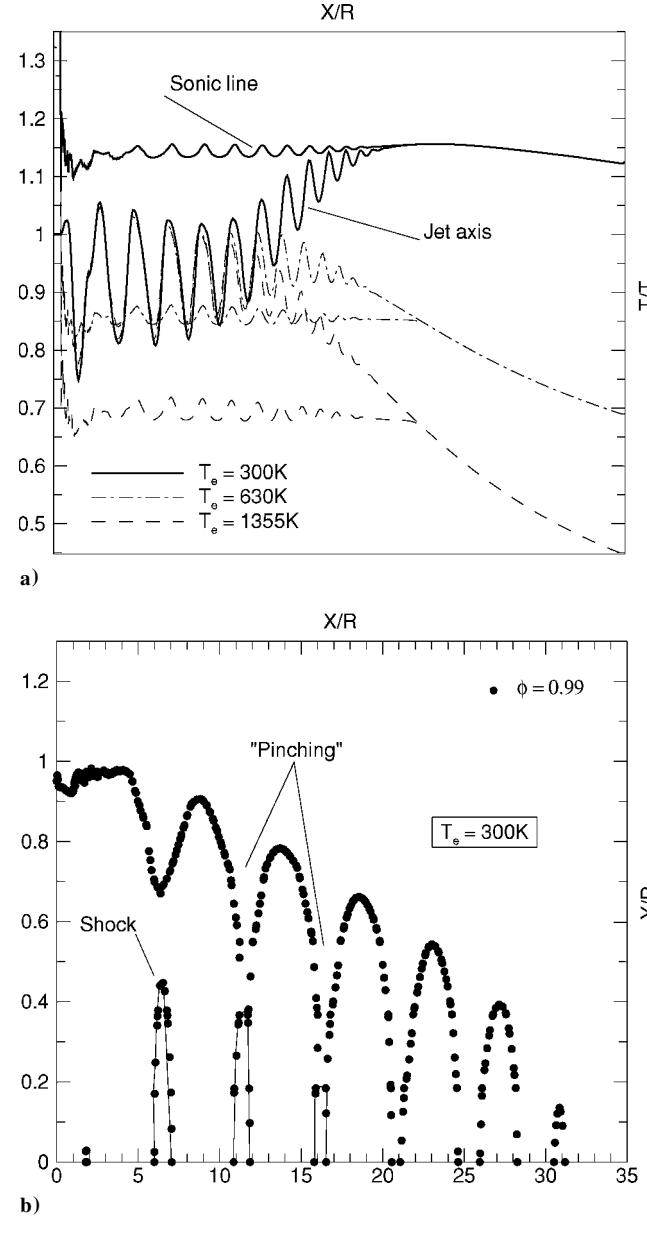

Fig. 8 Temperature along the axis and the sonic line; lower edge of the mixing layer.

supersonic part does not experience the outer flow condition, the sonic line properties remain almost constant; the amount of heat dissipation between the lower edge of the mixing layer and this constant free boundary may be given back to the jet core when the flow reaches the sonic condition [at $X/R \sim 52$ for the isothermal case (Fig. 8a)].

To follow the lower edge of the mixing layer, a mixing variable has been defined:

$$\phi = (U - U_a)/(U_e - U_a) \tag{18}$$

where U_a and U_e are the unmixed values of the coflow and jet velocities. From a theoretical viewpoint, the initial mixing zone may be defined as the zone where the velocity is equal to or greater than the exit one, or where $\phi \leq 0.99$. Figure 8b shows the location of the lower edge of the mixing layer for the 300-K jet. It is shown that this line oscillates in phase with the shock reflection pattern, involving some pinchings to the jet axis. From $X/R \sim 21$, these pinchings make the mixing layer come to lap the jet centerline (Fig. 8b), which involves some turbulent fluid being injected at each pinching, giving rise to the transition of the initial mixing zone (Fig. 7a). In addition, at each pinching, some hotter fluid coming from the viscous dissipation is also injected into the jet core and boosts the temperature after a compression (Fig. 8a).

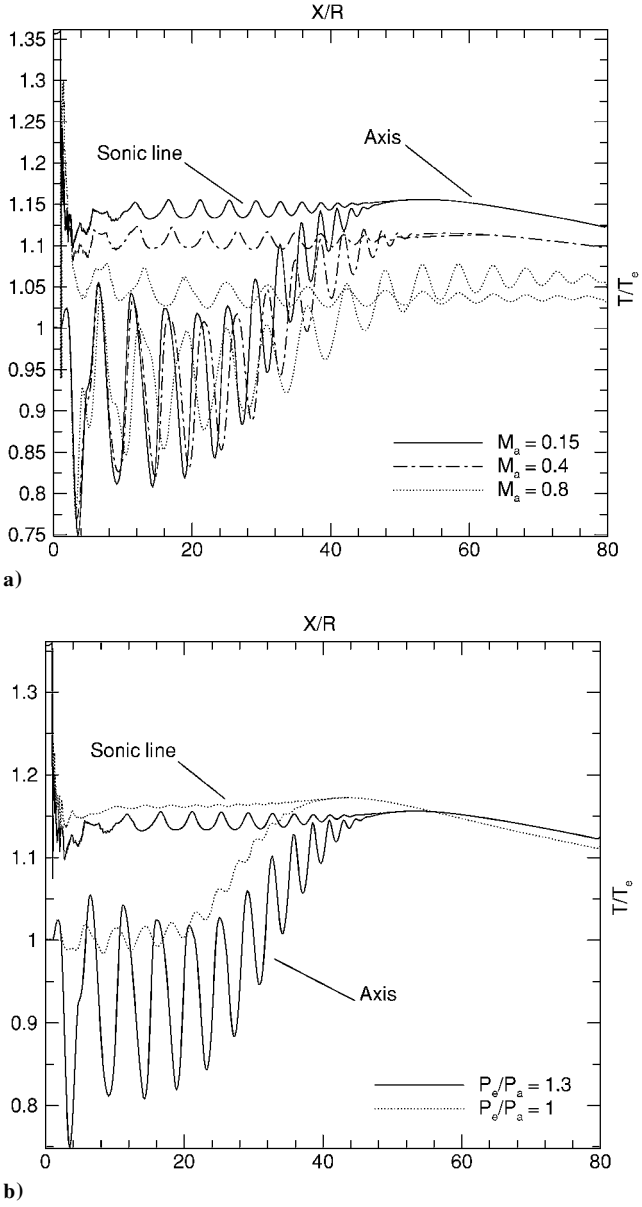

Fig. 9 Effect of the coflow Mach number and pressure ratio.

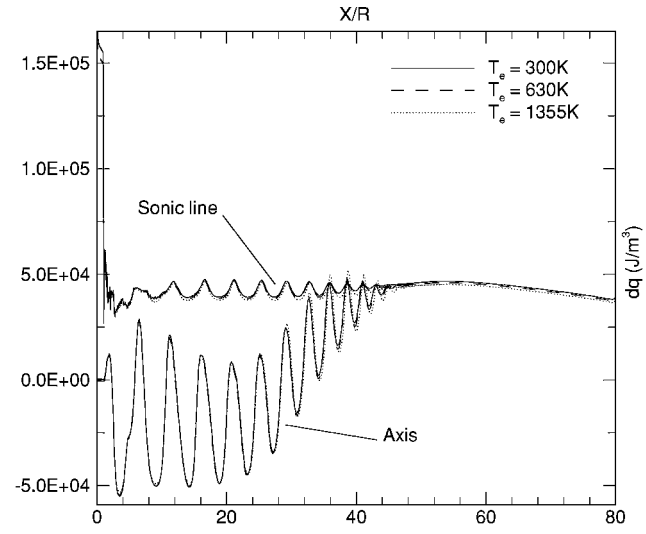

Fig. 10 Heat quantity variation for the jet and the sonic line.

Figures 9a and 9b show the effect of the coflow Mach number and the pressure ratio on the temperature increase effect for the isothermal jet. As the coflow Mach number increases, the maximum temperature decreases (Fig. 9a) because the heat dissipation effect is less important. In addition, when the flight Mach number is increased, the turbulence level and then the mixing are reduced, which causes the shocks to be less damped and allows the centerline temperature to be higher than that of the sonic line (Fig. 9a). When the jet is perfectly expanded (Fig. 9b), no expansions and compressions occur, but just wavelets[37] are visible. In that case, the thermal equilibrium in the mixing layer involves a higher temperature than that in the underexpanded case. The maximum temperature is then slightly higher for $P_e/P_a = 1$ than for $P_e/P_a = 1.3$.

Finally, the jet and coflow static temperatures have been increased to obtain isothermal jets with different temperatures (Fig. 10). For this test, the pressure ratio is still $P_e/P_a = 1.3$, and the shear stress between both flows is kept constant at all temperatures. Figure 10 shows that the quantity of heat received from the nozzle outlet, by the jet centerline and the sonic line, is constant for the three temperatures. This clearly shows that the heat dissipation effect is probably the most important parameter that drives the temperature increase observed in isothermal jets. Consequently, this aspect may not be attributed to a reversible transformation of kinetic energy into thermal energy, unlike what may happen during slight expansions and compressions in compressible flows. Indeed, in the latter case, the temperature may rise because $C_pT + V^2/2$ may be considered as constant along a streamline if the flow is adiabatic and reversible (no viscous work).

VII. Conclusions

In this work, underexpanded jets have been investigated with a fully elliptic Navier–Stokes equations solver, in conjunction with an adaptive unstructured mesh and a compressibility corrected RSM. Although this turbulence model has been used in the past for modeling compressible flows,[14,15] it has not been extensively used for underexpanded jets. The validation part has demonstrated that the model is in good agreement with experimental data as far as the dynamic characteristics are concerned for the both kinds of jets. In addition, it has been shown that there is improvement over k–ϵ models for turbulence predictions such as turbulent intensities or Reynolds stresses, which are important in the mixing layer modeling.

Moreover, the coupling between dynamic characteristics and the heat transfer has been studied for mildly underexpanded jets. The sonic line location has been revealed as a primary parameter for this analysis. It has been shown that a fraction of energy, lost in viscous dissipation, may be given back to the flow, which may lead to an optimum temperature zone for isothermal jets. This irreversible energy transfer and the flow transition have been explained as being due to the coupling between turbulence and compressibility, which gives rise to pinchings of the lower edge of the mixing layer. This

observation may be useful for spraying application, where the particles' temperature is a driving parameter of the coating. However, some measurements are necessary and will be performed to further investigate the thermal processes in these jets.

Acknowledgments

The authors acknowledge the financial support of the National Sciences and Engineering Research Council of Canada. They also acknowledge the contribution of Peter Lanigan for the reviewing and correction of the draft manuscript.

References

[1]Dash, S., Pergament, H., and Thorpe, R., "Computational Models for the Viscous/Inviscid Analysis of Jet Aircraft Exhaust Plumes," NASA, CR 3289, 1980.

[2]Rebaine, A., "Simulation d'Écoulements Internes Compressibles Laminaire et Turbulents par une Méthode d'Éléments Finis," Ph.D. Dissertation, Mechanical Engineering Dept., Univ. de Sherbrooke, Sherbrooke, QC, Canada, Feb. 1997.

[3]Cumber, P., Fairweather, M., Falle, S., and Giddings, J., "Predictions of the Structure of Turbulent, Moderately Underexpanded Jets," *Journal of Fluids Engineering*, Vol. 116, Dec. 1994, pp. 707–713.

[4]Cumber, P., Fairweather, M., Falle, S., and Giddings, J., "Predictions of the Structure of Turbulent, Highly Underexpanded Jets," *Journal of Fluids Engineering*, Vol. 117, Dec. 1994, pp. 599–604.

[5]Dash, S., Wolf, D., and Seiner, J., "Analysis of Turbulent Underexpanded Jets, Part 2: Shock Noise Features Using SCIPVIS," *AIAA Journal*, Vol. 23, No. 5, 1985, pp. 669–677.

[6]Pfender, E., Spores, R., and Chen, W., "A New Look at the Thermal and Gas Dynamic Characteristics of Plasma Jet," *International Journal of Material and Product Technology*, Vol. 10, No. 3–6, 1995, pp. 548–565.

[7]Jodoin, B., Proulx, P., and Mercadier, Y., "Numerical Study of Supersonic Direct Current Plasma Torch," *AIAA Journal*, Vol. 36, No. 4, 1998, pp. 578–584.

[8]Pao, S. P., and Abdol-Hamid, K., "Numerical Simulation of Jet Aerodynamics Using the Three-Dimensional Naviers–Stokes Code PAB3D," NASA TP 3596, 1996.

[9]Abdol-hamid, K., and Wilmoth, R., "Multiscale Turbulence Effects in Underexpanded Supersonic Jets," *AIAA Journal*, Vol. 27, No. 3, 1989, pp. 315–322.

[10]Dash, S., Wolf, D., and Seiner, J., "Analysis of Turbulent Underexpanded Jets, Part 1: Parabolized Navier–Stokes Model, SCIPVIS," *AIAA Journal*, Vol. 23, No. 4, 1985, pp. 505–514.

[11]Gribben, B., Badcock, K., and Richards, B., "Numerical Study of Shock-Reflection Hysteresis in an Underexpanded Jet," *AIAA Journal*, Vol. 38, No. 2, 2000, pp. 275–283.

[12]Rodi, W., "The Prediction of Free Turbulent Boundary Layers by the Use of a Two-Equation Model of Turbulence," Ph.D. Dissertation, Imperial College, London, 1972.

[13]Pope, S., "An Explanation of the Turbulent Round Jet/Plane Jet Anomaly," *AIAA Journal*, Vol. 16, No. 3, 1978, pp. 279–281.

[14]Chenault, C., and Beran, P., "K–e and Reynolds Stress Turbulence Model Comparisons for Two-Dimensional Injection Flows," *AIAA Journal*, Vol. 36, No. 8, 1998, pp. 1401–1412.

[15]Chenault, C., Beran, P., and Bowersox, R., "Numerical Investigation of Supersonic Injection Using a Reynolds-Stress Turbulence Model," *AIAA Journal*, Vol. 37, No. 10, 1999, pp. 1257–1269.

[16]Mehta, R., and Prasad, J., "Estimation of Shock-Cell Structure of Axisymmetric Supersonic Free Jets," *Indian Journal of Engineering and Materials Sciences*, Vol. 3, Aug. 1996, pp. 141–147.

[17]Prudhomme, S., and Haj-Hariri, H., "Investigation of Supersonic Underexpanded Jets Using Adaptative Unstructured Finite Elements," *Finite Elements in Analysis and Design*, Vol. 17, 1994, pp. 21–40.

[18]Desh, S., and Wolf, D., "Interactive Phenomena in Supersonic Jet Mixing Problems, Part 1: Phenomenology and Numerical Modeling Techniques," *AIAA Journal*, Vol. 22, No. 7, 1984, pp. 905–913.

[19]Donaldson, C., and Snedeker, R., "A Study of Free Jet Impingement. Part I. Mean Properties of Free and Impinging Jets," *Journal of Fluid Mechanics*, Vol. 45, 1971, pp. 281–319.

[20]Fox, J., "On the Structure of Jet Plumes," *AIAA Journal*, Vol. 12, No. 1, 1974, pp. 105–107.

[21]Abbett, M., "The Mach Disk in Underexpanded Exhaust Plumes," AIAA Paper 70-231, 1970.

[22]Abbett, M., "Mach Disk in Underexpanded Exhaust Plumes," *AIAA Journal*, Vol. 9, No. 3, 1971, pp. 512–514.

[23]Hagen, K., *Heat Transfer with Applications*, Prentice–Hall, Columbus, OH, 1999.

[24]Vargaftik, N., *Tables of the Thermophysical Properties of Liquids and Gases*, 2nd ed., Wiley, New York, 1975.

[25]Bartosiewicz, Y., Proulx, P., and Mercadier, Y., "Modeling of Turbulent Supersonic Underexpanded Jets," *Proceedings of the 8th Annual Conference of the CFD Canada*, Vol. 2, CERCA, Montreal, 2000, pp. 953–958.

[26]Lien, F., and Leschziner, M., "Assessment of Turbulent Transport Models Including Non-linear RNG Eddy Viscosity Formulation and Second-Moment Closure," *Computers and Fluids Journal*, Vol. 23, No. 8, 1994, pp. 983–1004.

[27]Fu, B., and Leschziner, M., "Modeling Strongly Swirling Recirculating Jet Flow with Reynolds-Stress Transport Closures," *Sixth Symposium on Turbulent Shear Flows*, Toulouse, France, 1987.

[28]Sarkar, S., and Balakrishnan, L., "Application of a Reynolds-stress Turbulence Model to the Compressible Shear Layer," NASA CR 182002, ICASE, Rept. 90-18, Hampton, VA, 1990.

[29]Sarkar, S., Erlebacher, G., Hssaini, M., and Kreiss, H., "The Analysis and Modeling of Dilatational Terms in Compressible Turbulence," *Journal of Fluid Mechanics*, Vol. 227, 1991, pp. 669–677.

[30]Papamoschou, D., and Roshko, A., "Observations of Supersonic Free Shear Layers," AIAA Paper 86-062, 1986.

[31]Roe, P., "Characteristic Based Schemes for the Euler Equations," *Annual Review of Fluid Mechanics*, Vol. 18, 1986, pp. 337–365.

[32]Roe, P., "Approximate Riemann Solvers, Parameter Vectors, and Difference Schemes," *Journal of Computational Physics*, Vol. 43, 1981, pp. 357–372.

[33]Weiss, J., Maruszewski, W., and Smith, W., "Implicit Solution of the Navier–Stokes Equations on Unstructured Meshes," AIAA Paper 97-2103, July 1997.

[34]Warren, G., Anderson, W., Thomas, J., and Krist, S., "Grid Convergence for Adaptative Methods," AIAA Paper 91-1592, 1991.

[35]Love, E., Grisby, C., Lee, L., and Wooldling, M., "Experimental and Theoretical Studies of Axisymmetric Free Jets," NASA TR R-6, 1959.

[36]Ashkenas, H., and Sherman, F., "The Structure and Utilization of Supersonic Free Jets in Low Density Wind Tunnel," *International Symposium on Rarified Gas Dynamics*, Vol. 2 (Supplement 3), Karlsruhe, Germany, 1966, pp. 84–105.

[37]Mclaughlin, D., Seiner, J., and Liu, C., "On the Noise Generated by Large Scale Instabilities in Supersonic Jets," AIAA Paper 80-0964, 1980.

M. Sichel
Associate Editor